

Hetero-/homogeneous combustion of fuel-lean $\text{CH}_4/\text{O}_2/\text{N}_2$ mixtures over PdO at elevated pressures

Ran Sui, John Mantzaras*, Et-touhami Es-sebbar, Rolf Bombach

Laboratory of Thermal Processes and Combustion, Paul Scherrer Institute (PSI), CH-5232 Villigen, Switzerland

Received 28 November 2017; accepted 25 May 2018

Available online 23 June 2018

Abstract

The heterogeneous and homogeneous combustion of fuel-lean $\text{CH}_4/\text{O}_2/\text{N}_2$ mixtures over PdO was investigated experimentally and numerically at equivalence ratios $\varphi = 0.27$ – 0.44 , pressures 1–12 bar and surface temperatures 710–1075 K. In situ Raman measurements of major gas-phase species concentrations across the boundary layer of a channel-flow catalytic reactor assessed the heterogeneous reactivity, while planar laser induced fluorescence (LIF) of the OH radical monitored homogeneous combustion. Simulations were performed using a 2-D code with detailed heterogeneous and homogeneous reaction mechanisms. Comparisons between Raman-measured and predicted transverse profiles of major species mole fractions attested the atmospheric-pressure suitability of a detailed surface mechanism and allowed for the construction of a global catalytic step valid in the range 1–12 bar. The methane catalytic reaction rate exhibited an overall pressure dependence $\sim p^{1-n}$ where the exponent n was itself a monotonically increasing function of pressure, rising from 0.58 at 3 bar to 1.02 at 12 bar. This resulted in a non-monotonic pressure dependence of the catalytic reaction rate in the range 1–12 bar, a behavior in stark contrast to other noble metals (Pt and Rh) where the methane reaction rates always increased with rising pressure. Surface temperatures remained well-below the PdO decomposition temperature at each corresponding pressure, owing largely to the “self-regulating” temperature effect of PdO, and this in turn mitigated homogeneous ignition. Simulations using the PdO decomposition temperatures as boundary conditions for the wall temperatures were further performed for practical CH_4 /air catalytic reactors in power generation systems. It was shown that for $p < 7$ bar (a range relevant to microreactors) homogeneous ignition was altogether suppressed. For higher pressures relevant to gas-turbine burners, however, gaseous combustion ought to be considered in the reactor design.

© 2018 The Combustion Institute. Published by Elsevier Inc. All rights reserved.

Keywords: Catalytic combustion of CH_4 on PdO; High-pressure CH_4 combustion; Pressure-dependence of CH_4 catalytic reactivity on PdO; In situ Raman and LIF; Homogeneous ignition of CH_4 over PdO

1. Introduction

The total oxidation of methane over palladium-based catalysts is of key importance for pollutant abatement in natural-gas-driven vehicles [1,2], for gas turbines employing hybrid hetero-/

* Corresponding author.

E-mail address: ioannis.mantzaras@psi.ch
(J. Mantzaras).

Two horizontal Si[SiC] ceramic plates (length 300 mm ($-x$), width 104 mm ($-z$), thickness 9 mm, positioned 7 mm apart ($-y$)) and two 3-mm-thick vertical quartz windows formed the channel reactor (Fig. 1). Using plasma vapor deposition (PVD), the inner Si[SiC] surfaces were coated first by a 1.5- μm -thick non-porous Al_2O_3 layer and then by a 2.2- μm -thick Pd layer. Such thick noble metal layers resembled polycrystalline surfaces. This was verified by X-ray photoelectron spectroscopy (XPS), which attested the absence of Al or Si from the catalyst surfaces [30].

Over the length $100 < x < 300$ mm, two adjustable-power resistive coils (positioned above/below the Si[SiC] plates) regulated the surface temperatures (Fig. 1(b)). The reactor was mounted inside a high-pressure cylindrical steel tank. Two 350-mm-long, 50-mm-high and 35-mm-thick quartz windows on the sides of the high-pressure tank provided a lateral ($-z$) optical access (Fig. 1(a)). Furthermore, two quartz windows at the rear tank flange and the reactor exhaust allowed for a streamwise ($-x$) optical access. On each plate, 12 S-type thermocouples (along the x - y symmetry plane, with their beads embedded 0.9 mm beneath the catalyst) monitored the surface temperatures. At the channel inlet ($x = 0$, position “A” in Fig. 1(b)) the gas temperature was measured by a K-type sheathed thermocouple. To better control the surface temperatures, in addition to the heating coils two cooling air-jets with adjustable flows issuing from two slots (10×100 mm² in x - z , located at $x = 30$ mm) impinged on the outer Si[SiC] surfaces (Fig. 1(b)).

Pressurized bottles supplied CH₄ (99.95%), O₂ and N₂, with their flows regulated by three Brooks mass flowmeters. O₂ and N₂ were mixed and then electrically preheated (Fig. 1(b)). Methane was injected to the preheated O₂/N₂ flow in a 200-mm-long steel conical section using eight 0.5-mm-diameter nozzles arranged laterally ($-z$ direction, Fig. 1(b)). The conical section had an ending cross-flow area equal to that of the channel (104×7 mm²). A wire mesh and two fine grids (0.5 mm² open areas) produced good mixing of CH₄ with O₂/N₂ and uniform exit velocity. At the exit plane of the conical section, hot wire velocimetry assessed the flow uniformity while planar LIF of NO (doped into CH₄, excitation at 226.25 nm, detection at 240–265 nm) verified the good mixing quality.

2.2. Laser-based measurements

A frequency-doubled pulsed Nd:YLF laser (Quantronix Darwin-Duo, 526.5 nm, 120 ns pulse, 40 mJ energy/pulse, 2 kHz repetition rate) provided the Raman excitation (Fig. 1(a)). A cylindrical lens ($f = 150$ mm) focused the laser beam into a ~ 0.3 mm thick vertical line extending over the 7 mm channel height. The focused light-line was laterally offset ($z = 15$ mm) to increase the collection angle and to diminish thermal beam steering [30,31]. The Raman-scattered light was focused by two spherical lenses ($f = 300$ mm, $f/4$) into the entrance slit of a 25 cm imaging spectrograph (Chromex-250i) connected to an intensified CCD camera (Princeton-Instruments PI-MAX1024GIII, 715×255 pixels corresponding to spectral shift and y -distance, respectively). A tilted Kaiser-Optical-Systems holographic notch filter at 532 nm and an OG550 Schott colored glass filter suppressed the excitation radiation.

The laser and spectrograph were mounted on an optical table (Fig. 1(a)), axially-traversable over $8 \leq x \leq 120$ mm. As the conditions were steady and laminar, scattered light from 300,000 laser pulses was integrated on the detector chip to increase the signal-to-noise ratio. The 7 mm channel-height was recorded on 220 pixels, which were binned to 64 pixels. Effective Raman cross-sections, which included transmission efficiencies (windows, lenses, spectrometer, filters and camera), were evaluated by recording the signals of several pressurized CH₄, N₂ and CO₂ containing mixtures, air, and the actual feed mixtures, as in [30]. The measurement accuracy was $\pm 3\%$ for concentrations $\geq 3\%$ volume and $\pm 8\%$ for concentrations as low as 0.5% volume. Raman data within typically 0.5–0.7 mm from both catalytic walls were discarded because of low signal-to-noise ratios.

For planar OH-LIF, a frequency-doubled pulsed Nd:YAG laser (Quantel YG781C20 CL-D-LNE3, 532 nm, pulse duration 10 ns, repetition rate 20 Hz) pumped a Quantel TDL90-NBP2EWT UVT3 dye laser (90% Rhodamine 6G and 10% Rhodamine B dye in ethanol). The output radiation was frequency-doubled at 283.05 nm to excite the A-X(1,0) Q₁(7) transition of OH. The excitation beam was transformed by a telescopic lens system and a slit into a vertical light sheet propagating counterflow along the x - y symmetry plane (Fig. 1(a)). An intensified CCD camera (LaVision Imager Compact HiRes-IRO, 1392×1024 pixels binned to 696×512) recorded the fluorescence at 90° through the reactor and tank side-windows. Fluorescence from both (1–1) and (0–0) transitions (308 and 314 nm, respectively) was collected. Areas 100×7 mm² were recorded on 1360×120 pixels of the CCD.

2.3. Surface science measurements

X-ray Photoelectron Spectroscopy (XPS) and Scanning Electron Microscopy (SEM) determined the palladium phases and surface morphology, respectively, of the fresh and used (after combustion tests at 955 K) catalysts. The XPS spectra in Fig. 2 indicated predominantly metallic Pd and oxidized PdO phases in the fresh and used samples, respectively. This was verified by the 3d_{5/2} and 3d_{3/2} transitions in Fig. 2 (3d_{5/2} was located at 335.2 and 337.2 eV for Pd and PdO, respectively, while 3d_{3/2} at 340.5 and 342.5 eV for Pd and PdO, respectively). As expected, at fuel-lean conditions combustion oxidized the Pd surface to PdO. The SEM images in Fig. 2 revealed a surface morphology developing from polycrystalline (fresh sample) to a porous layer (used sample), as also reported in the Pd wires of Xin et al. [24]. Atomic Force Microscopy (AFM) determined that the average surface protrusions in the fresh and used samples were 0.14 μ m and 1.62 μ m, respectively (see Supplemental Fig. S1).

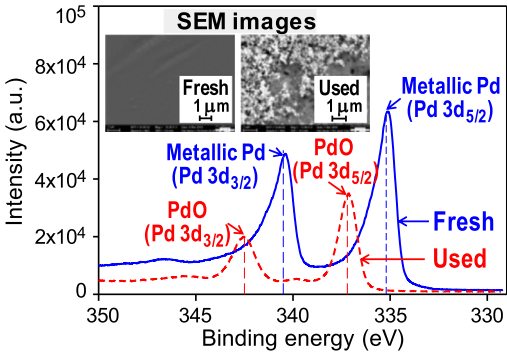


Fig. 2. XPS spectra of the fresh and used catalyst. Insets show corresponding SEM images.

3. Numerical

A 2-D steady Navier–Stokes CFD code [30] was used. A staggered grid with 480×68 points (in x and y , respectively) for the $300 \times 7 \text{ mm}^2$ domain along the x – y symmetry plane produced grid-independent solutions. Curves fitted through the 12 thermocouple measurements on each Si[SiC] plate yielded the lower-wall ($y = 0$) and upper-wall ($y = 7 \text{ mm}$) temperature profiles, which were then imposed as boundary conditions. The axial velocity, temperature, and species mass fractions at the inlet were uniform.

For methane total oxidation on PdO, the mechanism by Shimizu and Wang [23] was used (8 surface and 10 gaseous species, 26 reactions, surface site density $1.95 \times 10^{-9} \text{ mol/cm}^2$). For gas-phase chemistry, the $\text{C}_1/\text{H}/\text{O}$ elementary mechanism by Warnatz et al. [32] was employed (25 species, 108 reactions). Surface and gas-phase chemical reaction rates were evaluated using Chemkin [33,34]. Mixture-average diffusion was used together with the Chemkin transport database [35].

4. Results and discussion

Pressures 1–12 bar and equivalence ratios $\varphi = 0.27$ – 0.44 were investigated (Table 1). The flows were laminar with inlet Reynolds numbers (based on the channel height) $Re_{IN} = 650$ – 1150 . Before each test, the catalyst was oxidized in a 380 K air-flow for 30 min.

4.1. Assessment of catalytic reactivity

Comparisons between Raman-measured and predicted transverse profiles of CH_4 and H_2O mole fractions at five axial positions are presented in Fig. 3 (1 bar) and Fig. 4 (3 bar); for clarity, up to 20 of the total 64 data points are shown over the experimentally-resolvable channel height $0.6 \lesssim y \lesssim 6.4 \text{ mm}$. The corresponding wall temperature profiles are shown in Fig. 5(a). As will be elaborated in

Table 1
Experimental conditions.

Case ^a	p	φ	U_{IN}	T_{IN}	CH_4	O_2
1	1	0.43	3.73	439	5.4	25.0
2	1	0.44	4.26	439	5.4	24.8
3	3	0.35	1.61	438	4.9	27.8
4	3	0.40	1.21	430	5.0	25.2
5	5	0.27	0.92	440	5.5	40.7
6	5	0.40	0.72	427	6.0	30.0
7	8	0.29	0.51	444	5.8	39.6
8	8	0.40	0.52	445	6.0	30.0
9	10	0.30	0.41	426	5.9	39.9
10	10	0.40	0.41	441	6.0	30.0
11	12	0.30	0.24	426	5.9	39.9
12	12	0.39	0.33	374	5.2	26.4

^a Pressure (bar), equivalence ratio, inlet velocity (m/s), inlet temperature (K), CH_4 and O_2 vol. content (%), balance is N_2 .

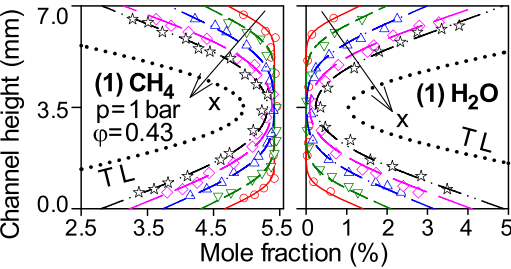


Fig. 3. Raman-measured (symbols) and predicted (lines) transverse profiles of methane and water mole fractions for Case 1; $x = 8 \text{ mm}$ (circles, solid lines), 21 mm (lower-triangles, short-dashed lines), 51 mm (upper-triangles, dashed-dotted lines), 81 mm (diamonds, long-dashed lines), 111 mm (stars, dashed double-dotted lines). Dotted lines marked TL are transport-limited simulations at $x = 111 \text{ mm}$.

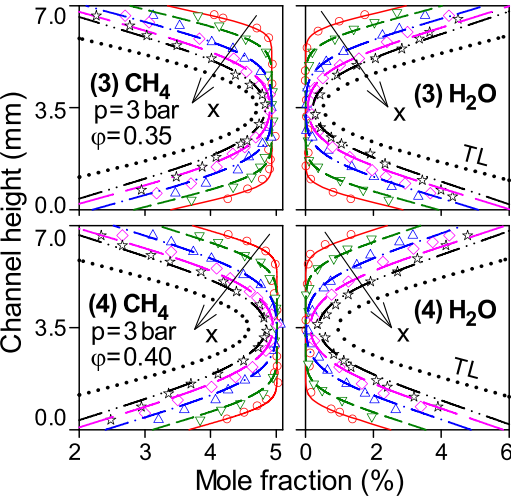


Fig. 4. Raman-measured (symbols) and predicted (lines) transverse profiles of methane and water mole fractions for Cases 3 and 4. Line and symbol notations as in Fig. 3.

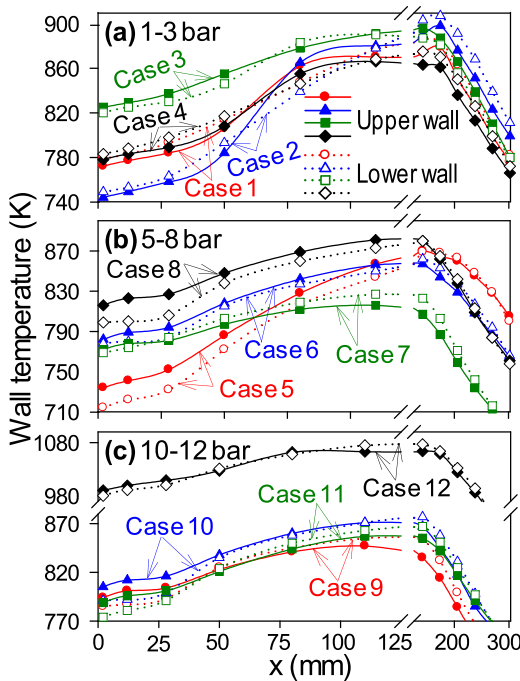


Fig. 5. Upper-wall and lower-wall measured temperatures for all cases.

Section 4.2, homogeneous combustion was absent in all cases. Hence, the CH_4 and H_2O transverse profiles shown in Figs. 3 and 4 (and hereafter) were solely established by catalytic chemistry (this was also confirmed by comparing simulations with and without including gaseous chemistry). The computed transport-limited (i.e., infinitely-fast surface chemistry) transverse profiles for the last axial position $x = 111$ mm are included in Figs. 3 and 4 (labeled “TL”). The TL profiles provided the physically attainable lowest (highest) bounds for the methane (water) mole fractions over the Raman-measured extent $8 \leq x \leq 111$ mm. The conditions in Figs. 3 and 4 clearly indicated a kinetically-controlled conversion, away from the transport limit (i.e., mole fractions of the deficient methane reactant well-above zero at both walls), which was a key requirement for assessing the catalytic reactivity. The wall temperatures for Case 1 and Cases 3, 4 over the axial distances of Figs. 3 and 4 were 772–886 K and 778–896 K, respectively (Fig. 5(a)).

Simulations at 1 bar in Fig. 3 agreed very well with the measurements at all axial positions. The simulations reproduced the measured CH_4 and H_2O mole fractions and the near-wall bending of these species. In particular, the transverse gradient of the deficient CH_4 reactant at the wall was a quantity directly linked to the local catalytic reactivity [30]. At 3 bar, however, deviations between simulations and measurements appeared, as

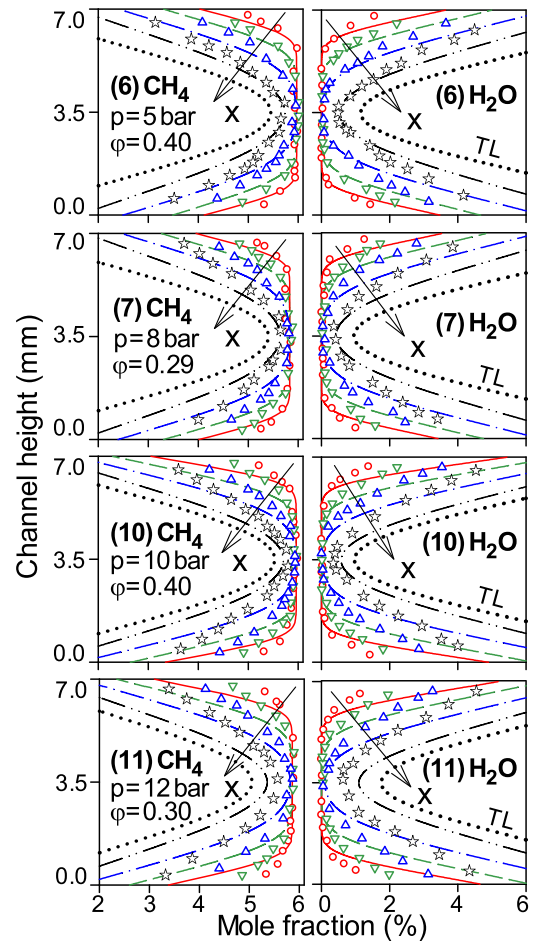


Fig. 6. Raman-measured (symbols) and predicted (lines) transverse profiles of CH_4 and H_2O mole fractions for selected cases at 5–12 bar; $x = 8$ mm (circles, solid lines), 21 mm (lower-triangles, short-dashed lines), 51 mm (upper-triangles, dashed-dotted lines), 111 mm (stars, dashed double-dotted lines). Dotted lines marked TL are transport-limited simulations at $x = 111$ mm.

evidenced at the last two axial locations (diamonds and stars in Fig. 4) whereby the catalytic reactivity was modestly overpredicted (lower computed near-wall CH_4 mole fractions and steeper bending of the computed CH_4 profiles).

The overprediction of the catalytic reactivity progressively aggravated with increasing pressure from 3 to 12 bar. This is evidenced in Fig. 6 where the predicted CH_4 (H_2O) mole fractions were substantially lower (higher) than the measurements. Characteristically, at $p = 5, 8, 10$ and 12 bar the predicted methane mole fractions in Fig. 6 were 27%, 36%, 50% and 56% lower than the corresponding measurements at the last x -position and topmost y -location (star symbols).

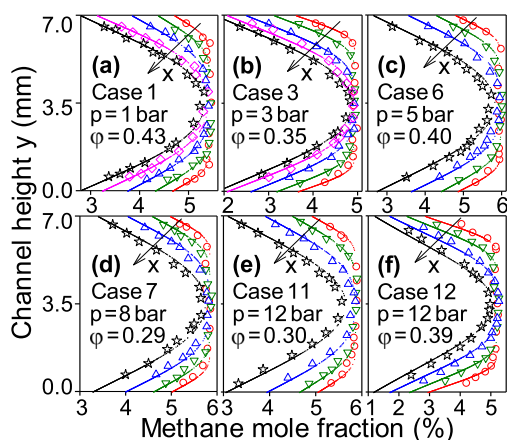


Fig. 7. Measured (symbols) and predicted (lines, using Eq. (1) with fitted kinetic parameters) methane mole fractions. Symbols notation as in Fig. 3.

Our previous investigations of fuel-lean methane/air oxidation over platinum [30] and rhodium [31] have shown that crucial for the high-pressure applicability of a catalytic reaction mechanism is its capacity to capture the reduction in surface free-site coverage (and the corresponding increase in oxygen coverage) with increasing pressure. This reduction, in turn, restrained the rate of increase of the catalytic reactivity with rising pressure. A one-step reaction for methane total oxidation, first-order with respect to methane was shown valid for Pt and Rh:

$$\dot{s}_{\text{CH}_4} = A(p/p_o)^{-n} \exp(-E_a/RT_w)[\text{CH}_4]_w, \quad (1)$$

with A the pre-exponential factor, p_o a reference pressure, E_a the effective activation energy, T_w the wall temperature, $[\text{CH}_4]_w$ the methane concentration at the gas–wall interface and \dot{s}_{CH_4} the methane catalytic molar reaction rate. For platinum $n = 0.53$ (valid over 1–16 bar, with $p_o = 1$ bar [30]) while for rhodium $n = 0.70$ (2–12 bar, with $p_o = 2$ bar [31]).

The positive exponent n decelerated the increase of the reaction rate with rising pressure, since $\dot{s}_{\text{CH}_4} \sim p^{1-n}$ (given that $[\text{CH}_4]_w \sim p$ in Eq. (1)). The global step in Eq. (1) with fitted parameters $E_a = 58$ kJ/mol, $A = 1.7 \times 10^4$ cm/s and $p_o = 1$ bar reproduced excellently the predictions of the detailed mechanism [23] at 1 bar and also the Raman measurements (see Fig. 7(a) and further compare with Fig. 3). The kinetic parameter fitting (A , E_a , and the confirmation of a nearly first-order methane dependence) was accomplished using the detailed surface mechanism [23] along with the surface perfectly stirred reactor (SPSR) code of Chemkin [36] at 1 bar and temperatures 700–950 K. Inclusion of H_2O inhibition in Eq. (1) was not necessary (as also in the atmospheric-pressure global step of [19]), since no water was added in the reactant feed and the catalytically-produced water was

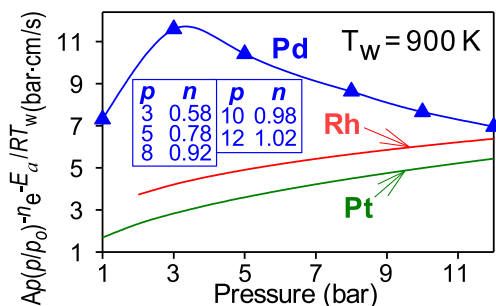


Fig. 8. Reaction rate parameter $Ap(p/p_o)^{-n}\exp(-E_a/RT_w)$ for Pd, Pt and Rh versus pressure.

modest. At elevated pressures the accelerated drop of the reaction rate with rising pressure necessitated a pressure-dependent exponent n . Simulations (see Fig. 7) were in quite good agreement with the Raman measurements for the deficient methane reactant at all pressures, when $n = 0.58$ (3 bar), 0.78 (5 bar), 0.92 (8 bar), 0.98 (10 bar) and 1.02 (12 bar).

For direct comparisons with Pt and Rh [30,31] Eq. (1) was recast, using $[\text{CH}_4]_w = pX_{\text{CH}_4,w}/RT_w$, to $\dot{s}_{\text{CH}_4}(RT_w/X_{\text{CH}_4,w}) = Ap(p/p_o)^{-n}\exp(-E_a/RT_w)$. Considering for all catalysts the same wall methane mole fraction, $X_{\text{CH}_4,w}$, and a common $T_w = 900$ K (a temperature where all three noble-metal global steps were applicable), the quantities $Ap(p/p_o)^{-n}\exp(-E_a/RT_w)$ which are directly proportional to the reaction rates \dot{s}_{CH_4} are compared in Fig. 8. The reactivity increased in the order Pt, Rh and Pd (as also reported in [7] for atmospheric-pressure). However, Pd exhibited a complex behavior: its reaction rate increased from 1 to 3 bar and then dropped monotonically.

The reactivity drop at high pressures was in qualitative agreement with two earlier studies on supported-Pd at $p \geq 5$ bar [28,29]. In both studies the linear velocity was constant when changing pressure (i.e., the mass throughput was constant). For Pd/ Al_2O_3 in [28] and for a fixed inlet temperature of 773 K, a pressure change from 5 to 15 bar at steps of 2.5 bar led to a monotonic drop of methane conversion ($\sim 70\%$ between 5 and 15 bar). A smaller drop in methane conversion over Pd-Mn catalysts with rising pressure was observed in [29], whereby only two pressures (5 and 12 bar) were studied for $T_{\text{IN}} \geq 850$ K; the corresponding drop was $\sim 25\%$ at 850 K and $\sim 50\%$ at 900 K. The reduction in methane conversion with rising pressure along with the constant mass flow rates in [28,29] indicated a pressure-induced kinetic inhibition. Very recently [37], first-principle (DFT) simulations and microkinetic modeling have revealed a non-monotonic dependence of the intrinsic methane catalytic reactivity on PdO over 1–10 bar, similar to the one observed in Fig. 8, albeit only for the temperature window

693–748 K. The simulations in [37] pertained to volumetric feed composition 1000 ppm CH₄, 10% O₂, 5% H₂O, 5% CO₂ and Ar balance. Therein, the non-monotonic behavior was attributed to the pressure-dependent coverages of the dominant surface species water, bicarbonates and hydroxyls.

4.2. Homogeneous combustion

Palladium catalysts are known to exhibit a “self-regulating” surface temperature effect due to the PdO decomposition [3]. The wall temperatures in all cases remained below the PdO decomposition temperature at the corresponding O₂ partial pressures (note, the % O₂ in Table 1 was always higher than that of air) even when attempting to run the plate heaters at full power and without air-cooling. This was likely a result of two factors: a drop in methane reactivity as the PdO decomposition temperature was approached, and the heat losses from the 9-mm-thick Si[SiC] plates towards the metal support frame (see Fig. 1(b)) that reduced the heat input from the resistive coils.

Despite the lower wall temperatures attained over Pd (compared to Pt or Rh where their nearly transport-limited methane conversion allowed for peak T_w above 1250 K [30,31]) that hindered homogeneous ignition, the large near-wall methane excess on Pd (see Fig. 7) should have promoted homogeneous ignition. The inhibition due to lower wall-temperature was stronger than the promotion due to higher near-wall methane concentration, leading to an overall suppression of homogeneous combustion. The absence of homogeneous combustion was attested by both simulations (using the one-step reaction of Eq. (1) together with the elementary gas-phase mechanism [32]) and LIF measurements (lack of OH signals). Since rising pressures favored homogeneous ignition [30], Case 12 was examined at the highest pressure ($p = 12$ bar) with full-power plate heating and no air cooling. As seen in Fig. 5(c) the wall temperatures still did not exceed 1078 K (the PdO decomposition temperature at the corresponding O₂ partial pressure was above 1200 K) and this was insufficient to ignite gaseous combustion. The global step of Eq. (1) also provided good agreement to the Raman measurements for Case 12 down to the last position $x = 111$ mm where $T_w = 1075$ K as illustrated in Fig. 7(f).

The homogeneous ignition propensity was assessed by performing simulations for 1–12 bar, a CH₄/air mixture at $\phi = 0.40$ and constant T_w equal to the PdO decomposition temperatures [10,11]. The catalytic step of Eq. (1) and the elementary gaseous mechanism were used to simulate a representative cylindrical channel of a monolithic reactor used for power generation having diameter 1.2 mm, length 50 mm [4], and a gas-turbine-relevant $T_{IN} = 750$ K. At $p_o = 1$ bar the inlet velocity was $U_{IN,p_o} = 4$ m/s, and to main-

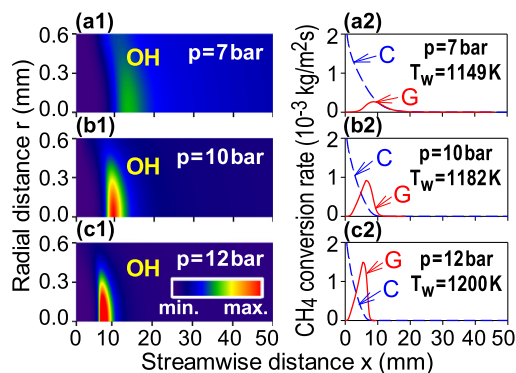


Fig. 9. (a1)–(c1) Computed 2-D OH maps in a cylindrical channel ($r = 0$: centerline, $r = 0.6$ mm: gas/wall interface). CH₄/air, $\phi = 0.4$, $T_{IN} = 750$ K and T_w equal to the PdO decomposition temperature at each pressure. Color bar provides OH levels (minima: 0 ppmv, maxima: (a1) 1.4, (b1) 6.8, and (c1) 22.4 ppmv). (a2)–(c2) Streamwise profiles of catalytic (C) and gaseous (G) methane conversion rates.

tain the same mass throughput at higher pressures $U_{IN,p} = U_{IN,p_o} \times (p_o/p)$. Figure 9 provides 2-D OH distributions and streamwise profiles of methane catalytic (C) and gaseous (G) conversions at three pressures. The G profiles were constructed by integrating over the channel radius the volumetric gaseous methane reaction rates. Gas-phase conversion was appreciable (amounting to more than 5% of the total methane conversion) only for $p \geq 7$ bar. Although the PdO decomposition temperatures used as T_w in the simulations of Fig. 9 in practical systems depended on the support material [8,15], the results indicated that for atmospheric pressure applications and for micro-turbine based microreactors with operating pressures up to 5 bar, gas-phase combustion was altogether suppressed.

5. Conclusions

The heterogeneous and homogeneous combustion of fuel-lean CH₄/O₂/N₂ mixtures over PdO was investigated at 1–12 bar and 710–1075 K. Comparisons between predicted and measured transverse profiles of gas-phase methane and water mole fractions attested the atmospheric-pressure suitability of a detailed surface reaction mechanism and allowed for the construction of a global catalytic step valid for 1–12 bar and 710–900 K. For the highest pressure $p = 12$ bar, the global step was further valid up to 1075 K. The catalytic reactivity of methane over PdO exhibited a pressure dependence $\sim p^{1-n}$ with a pressure-dependent exponent n , increasing from 0.58 at 3 bar to 1.02 at 12 bar. This resulted in a non-monotonic pressure dependence of the catalytic reaction rate for 1–12 bar, a

behavior opposite to that observed in other noble metals (Pt and Rh).

The attained surface temperatures remained below the PdO decomposition temperature and this mitigated homogeneous ignition. The developed global catalytic step together with an elementary gas-phase mechanism simulated CH₄/air combustion in practical power generation catalytic burners at various pressures and surface temperatures corresponding to the theoretical PdO decomposition temperatures. It was shown that for $p < 7$ bar (a range encompassing atmospheric pressure systems and microreactors) homogeneous ignition was suppressed. For gas-turbine systems, however, the potential of gaseous combustion must be considered for reactor design.

Acknowledgments

Support was given via the project EU-HRC. We thank J. Theile for helping the tests, and M. El Kazzi, E. De Boni and E.W. Burns for the XPS, SEM and AFM measurements.

Supplementary materials

Supplementary material associated with this article can be found, in the online version, at doi:10.1016/j.proci.2018.05.112.

References

- [1] J.K. Lampert, M.S. Kazi, R.J. Farrauto, *Appl. Catal. B* 14 (1997) 211–223.
- [2] M. Hussain, F.A. Deorsola, N. Russo, D. Fino, R. Pirone, *Fuel* 149 (2015) 2–7.
- [3] T. Griffin, W. Weisenstein, V. Scherer, M. Fowles, *Combust. Flame* 101 (1995) 81–90.
- [4] R. Carroni, T. Griffin, J. Mantzaras, M. Reinke, *Catal. Today* 83 (2003) 157–170.
- [5] G. Arzamendi, P.M. Dieguez, M. Montes, J.A. Odriozola, E.F. Sousa-Aguiar, L.M. Gandia, *Chem. Eng. J.* 154 (2009) 168–173.
- [6] R. Sui, Et. Es-sebbar, J. Mantzaras, N. Prasianakis, *Combust. Sci. Technol.* 190 (2018) 336–362.
- [7] M. Lyubovsky, L.L. Smith, M. Castaldi, et al., *Catal. Today* 83 (2003) 71–84.
- [8] R.J. Farrauto, J.K. Lampert, M.C. Hobson, E.M. Waterman, *Appl. Catal. B* 6 (1995) 263–270.
- [9] J.G. McCarty, *Catal. Today* 26 (1995) 283–293.
- [10] R.A. Dalla Betta, J.C. Schlatter, S.G. Nickolas, et al., *J. Eng. Gas Turbines Power* 119 (1997) 844–851.
- [11] H. Zhang, J. Gromek, G.W. Fernando, S. Boorse, H.L. Marcus, *J. Phase Equilib.* 23 (2002) 246–248.
- [12] F.H. Ribeiro, M. Chow, R.A. Dalla Betta, *J. Catal.* 146 (1994) 537–544.
- [13] M. Lyubovsky, L. Pfefferle, *Catal. Today* 47 (1999) 29–44.
- [14] G.H. Zhu, J.Y. Han, D.Y. Zemlyanov, F.H. Ribeiro, *J. Am. Chem. Soc.* 126 (2004) 9896–9897.
- [15] H. Yoshida, T. Nakajima, Y. Yazawa, T. Hattori, *Appl. Catal. B* 71 (2007) 70–79.
- [16] I. Czekaj, K.A. Kacprzak, J. Mantzaras, *Phys. Chem. Chem. Phys.* 15 (2013) 11368–11374.
- [17] Q. Mao, A.C.T. van Duin, K.H. Luo, *Proc. Combust. Inst.* 36 (2017) 4339–4346.
- [18] M.M. Wolf, H.Y. Zhu, W.H. Green, G.S. Jackson, *Appl. Catal. A* 244 (2003) 323–340.
- [19] S.T. Kolaczowski, W.J. Thomas, J. Titiloye, D.J. Worth, *Combust. Sci. Technol.* 118 (1996) 79–100.
- [20] G. Groppi, W. Ibashi, M. Valentini, P. Forzatti, *Chem. Eng. Sci.* 56 (2001) 831–839.
- [21] D. Ciuparu, M.R. Lyubovsky, E. Altman, L.D. Pfefferle, A. Datye, *Cat. Rev. – Sci. Eng.* 44 (2002) 593–649.
- [22] G.H. Zhu, J.Y. Han, D.Y. Zernlyanov, F.H. Ribeiro, *J. Phys. Chem. B* 109 (2005) 2331–2337.
- [23] T. Shimizu, H. Wang, *Proc. Combust. Inst.* 33 (2011) 1859–1866.
- [24] Y.X. Xin, S. Lieb, H. Wang, C.K. Law, *J. Phys. Chem. C* 117 (2013) 19499–19507.
- [25] T.C. Zhang, Y.X. Xin, Z.Y. Ren, F. Qi, C.K. Law, *Combust. Flame* 160 (2013) 149–154.
- [26] Y.X. Xin, H. Wang, C.K. Law, *Combust. Flame* 161 (2014) 1048–1054.
- [27] R.W. Sidwell, H. Zhu, R.J. Kee, D.T. Wickham, C. Schell, G.S. Jackson, *Proc. Combust. Inst.* 29 (2002) 1013–1020.
- [28] K. Persson, A. Ersson, A.M. Carrera, et al., *Catal. Today* 100 (2005) 479–483.
- [29] J. Requies, M.C. Alvarez-Galvan, V.L. Barrio, et al., *Appl. Catal. B* 79 (2008) 122–131.
- [30] M. Reinke, J. Mantzaras, R. Schaeren, R. Bombach, A. Inauen, S. Schenker, *Combust. Flame* 136 (2004) 217–240.
- [31] R. Sui, J. Mantzaras, R. Bombach, A. Denisov, *Proc. Combust. Inst.* 36 (2017) 4321–4328.
- [32] J. Warnatz, R.W. Dibble, U. Maas, *Combustion, Physical and Chemical Fundamentals, Modeling and Simulation*, Springer-Verlag, New York, 1996.
- [33] M.E. Coltrin, R.J. Kee, F.M. Rupley, *Surface Chemkin A Fortran Package for Analyzing Heterogeneous Chemical Kinetics at the Solid Surface-Gas Phase Interface*, Sandia National Laboratories, 1996 Report No. SAND90-8003C.
- [34] R.J. Kee, F.M. Rupley, J.A. Miller, *Chemkin II A Fortran Chemical Kinetics Package for the Analysis of Gas-Phase Chemical Kinetics*, Sandia National Laboratories, 1996 Report No. SAND89-8009B.
- [35] R.J. Kee, G. Dixon-Lewis, J. Warnatz, M.E. Coltrin, J.A. Miller, *A Fortran Computer Code Package for the Evaluation of Gas-Phase Multicomponent Transport Properties*, Sandia National Laboratories, 1996 Report No. SAND86-8246.
- [36] H.K. Moffat, R.J. Kee, J.F. Grear, J.A. Miller, *Surface PSR A Fortran Program for Modeling Well-Stirred Reactors with Gas and Surface Reactions*, Sandia National Laboratories, 1993 Report No. SAND91-8001.
- [37] C.-R. Florén, M. Van den Bossche, D. Creaser, et al., *Catal. Sci. Technol.* 8 (2018) 508–520.